RESEARCH ARTICLE

3D-printed HA15-loaded β-Tricalcium Phosphate/ Poly (Lactic-co-glycolic acid) Bone Tissue Scaffold Promotes Bone Regeneration in Rabbit Radial Defects

Chuanchuan Zheng[1†], Shokouh Attarilar[2†], Kai Li[3†], Chong Wang[4], Jia Liu[1*], Liqiang Wang[5], Junlin Yang[2], Yujin Tang[1*]

[1]Department of Orthopedics, Affiliated Hospital of Youjiang Medical University for Nationalities, Baise, Guangxi, 533000, China
[2]Department of Pediatric Orthopaedics, Xinhua Hospital Affiliated to Shanghai Jiao Tong University School of Medicine, Shanghai, 200092, China
[3]Academy of Orthopedics, Guangdong Province, Guangdong Provincial Key Laboratory of Bone and Joint Degeneration Diseases, The Third Affiliated Hospital of Southern Medical University, Guangzhou 510000, China.
[4]School of Mechanical Engineering, Dongguan University of Technology, Dongguan, Guangdong, 523808, China
[5]State Key Laboratory of Metal Matrix Composites, School of Material Science and Engineering, Shanghai Jiao Tong University, Shanghai, 200240, China
[†]*These authors contributed equally to this work.*

Abstract: In this study, a β-tricalcium phosphate (β-TCP)/poly (lactic-co-glycolic acid) (PLGA) bone tissue scaffold was loaded with osteogenesis-promoting drug HA15 and constructed by three-dimensional (3D) printing technology. This drug delivery system with favorable biomechanical properties, bone conduction function, and local release of osteogenic drugs could provide the basis for the treatment of bone defects. The biomechanical properties of the scaffold were investigated by compressive testing, showing comparable biomechanical properties with cancellous bone tissue. Furthermore, the microstructure, pore morphology, and condition were studied. Moreover, the drug release concentration, the effect of anti-tuberculosis drugs *in vitro* and in rabbit radial defects, and the ability of the scaffold to repair the defects were studied. The results show that the scaffold loaded with HA15 can promote cell differentiation into osteoblasts *in vitro*, targeting HSPA5. The micro-computed tomography scans showed that after 12 weeks of scaffold implantation, the defect of the rabbit radius was repaired and the peripheral blood vessels were regenerated. Thus, HA15 can target HSPA5 to inhibit endoplasmic reticulum stress which finally leads to promotion of osteogenesis, bone regeneration, and angiogenesis in the rabbit bone defect model. Overall, the 3D-printed β-TCP/PLGA-loaded HA15 bone tissue scaffold can be used as a substitute material for the treatment of bone defects because of its unique biomechanical properties and bone conductivity.

Keywords: Three-dimensional printing; β-tricalcium phosphate; HA15; Endoplasmic reticulum stress; Bone defect

***Correspondence to**: Yujin Tang, Department of Orthopedics, Affiliated Hospital of Youjiang Medical University for Nationalities, Baise, Guangxi, 533000, China; tangyujin1967@163.com. Jia Liu, Department of Orthopedics, Affiliated Hospital of Youjiang Medical University for Nationalities, Baise, Guangxi, 533000, China; liujia0111@live.cn

Received: October 30, 2020; **Accepted:** November 23, 2020; **Published Online:** January 20, 2021

Citation: Zheng C, Attarilar S, Li K, *et al*., 2021, 3D-printed HA15-loaded β-Tricalcium Phosphate/Poly (Lactic-co-glycolic acid) Bone Tissue Scaffold Promotes Bone Regeneration in Rabbit Radial Defects. *Int J Bioprint*, 7(1):317.http://doi.org/10.18063/ijb.v7i1.317

1. Introduction

Bone defects, which are of prominent importance, refer to a range of injuries that happen due to different reasons, including bone atrophy, trauma, benign and malignant tumors, and periodontal disease[1]. In this regard, an autologous bone graft is a unique standard of the hard tissue transplantation treatment, especially for bone defects[2].

These autologous bone grafts have numerous biological benefits over heterologous and synthetic bone substitutes due to their excellent combination of osteogenic, osteoinductive, and osteoconductive characteristics[3,4]. Despite these advantages, bone transplantation can lead to issues, such as bleeding, hematoma, infection, and chronic pains. Furthermore, this form of treatment is restrained by the donor sources and high costs of surgery[5,6]. Considering these issues and the great demand for treatment of bone defects, the need for modern designs and new strategies has been elevated to an urgent status, specifically for large-area bone defects. In this relation, bone tissue engineering is considered one of the most promising alternative approach for bone defect repairment[7]. One of the aims of bone tissue engineering is to fabricate osteoconductive scaffolds along with the successful delivery of osteogenic cells and biological factors[8].

The scaffold design should be able to accommodate living cells and guide their growth, and assist tissue regeneration in three dimensions[9,10]. The fabrication techniques also have a great impact on scaffold properties[11]. Moreover, the material and method selection must be designed according to specific demands of tissue (structural and metabolic)[12]. According to the biomimetic scaffold production protocols, the prepared scaffold must maintain a sufficient area for cell adhesion and proliferation, exchange of gaseous species, with the optimized surface-to-volume ratio and the degradation rate that matches tissue formation rate[13]. The scaffold's porosity, surface chemistry, morphology, three dimensional (3D) structure, immunogenicity, and mechanical properties have an extensive impact on the matrix properties in the biological artificial bone substitutes[14]. As yet, a wide array of materials has been used as matrix in bone tissue engineering, including natural polymers and their monomers (elastin, chitosan, silk, collagen, gelatin, etc.)[15], synthetic biodegradable polymers (polylactides, polycaprolactone, polypropylene fumarate, polyethylene glycol, etc.)[16], inorganic compounds of bone extracellular matrix (calcium phosphates, β-tricalcium phosphate [β-TCP], hydroxyapatite [HA], calcium carbonate, etc.)[17], and signaling molecules (RGD proteins and various growth factors)[18]. It was clear that bone tissue engineering scaffolds should imitate the composition and structure of natural bone tissue mostly by engaging biodegradable polymer matrix and inorganic bioactive fillers in 3D composite porous scaffolds.

The utilization of β-TCP and poly (lactic-co-glycolic acid) (PLGA) is very common due to their beneficial aspects. The β-TCP has found many applications in load-bearing orthopedic implants because of its compositional analogy to natural bone, osteoconductivity, and tailorable bioresorbability[19,20]. Furthermore, the PLGA is considered one of the base biomaterials because of its biocompatibility, potential for tailoring its biodegradation rate, Food and Drug Administration certification for clinical use in humans, surface modification ability, and the ease of export to other countries[21]. In addition, HA15 is an efficient inhibitor of endoplasmic reticulum (ER) chaperone protein glucose regulatory protein 78 (GRP78, also known as BiP), which can prohibit the ATPase activity of BiP and trigger the ER stress. Through ER stress, the cells activate unfolded protein response (UPR) and other signaling pathways in reaction to misfolded and unfolded protein aggregation in the ER cavity and the disorder of calcium balance.

Many stress responses can activate ER stress, thus could be called UPR[22-24]. UPR is mediated by three major signaling cascades that are triggered by the so-called ER pressure sensors, such as double-stranded RNA activated protein kinase R (like endothelial reticulum kinase [PERK]), inositol-dependent enzyme 1 α (IRE1 α), and activating transcription factor 6 (ATF6). PERK, IRE1 α, and ATF6 are ER membrane proteins, which are known to form complexes with BiP in a steady-state condition. The increased demand for protein folding leads to activation of PERK, IRE1 α, and ATF6, subsequently activating their downstream influencers to alleviate protein toxic stress on ER and restore ER homeostasis[25,26]. In this regard, HA15 can bind to the ATP enzyme of BiP and inhibit its activity, leading to BiP separation from PERK, IRE1 α, and ATF6 that elicits ER stress and UPR[27]. The dissociation of BiP can activate PERK that subsequently phosphorylates eIF2 α, leading to the inhibition of protein synthesis, which is conducive to the folding of proteins in the ER. Unlike most proteins, the phosphorylated eIF2 α selectively promotes the translation of ATF 4. Since the ATF4 has an upstream open reading frame in its fifth untranslated region, under normal circumstances, these upstream open reading frames would prevent the translation of ATF4. Phosphorylated eIF2 α can promote ribosome binding to the open reading frame of ATF4, inducing the expression of ATF4 mRNA and increasing the translation of ATF4. ATF4 and runt-related transcription factor 2 (Runx2) can interact with osteoblast-specific actin element 1 (OSE1) and osteoblast-specific actin element 2 (OSE2), respectively, in the osteocalcin (OCN) promoter region. This can induce the expression of osteoblast-specific OCN along with bone matrix mineralization promotion, osteoblast differentiation regulation, and bone formation[28,29]. Therefore, HA15 can promote osteoblast differentiation through the PERK-eIf2 α-ATF4 pathway. It was known that the accumulation of misfolded protein in the ER may lead to the secretion of HSPA5/BiP (GRP78) from ERN1/IRE1, allowing homodimerization and subsequent activation of ERN1/IRE1. This event has an auxiliary role in the post-translational transport of small presecretory proteins across the ER. Furthermore, the HSPA5 gene is overexpressed due to UPR under the cellular stress conditions[30-32]; therefore, the expression of

HSPA5 gene is a reliable indicator of ER stress in human diseases[33]. Furthermore, HSPA5 promotes cell survival and drug resistance under ER stress conditions[34]. Hence, it seems that β-TCP/PLGA-loaded HA15 material targeting HSPA5 which is a master regulator of the anti-apoptotic UPR signaling network[35] can be a good therapeutic option for bone defect problems.

In this study, we constructed a 3D-printed β-TCP/PLGA-loaded HA15 targeting HSPA5 bone tissue scaffold according to a rabbit model of radial bone defect and performed the implantation. The effect of 3D-printed β-TCP/PLGA-loaded HA15 bone tissue scaffold on bone defect treatment and the healing condition is thoroughly discussed in this article. This study also provides a theoretical and experimental guideline for the treatment of bone defect with drug-loaded biomaterials that may be a promising treatment of bone lesions.

2. Materials and methods

2.1. Scaffold fabrication

The 3D-printed bone tissue scaffold formation procedure along with *in vitro* and *in vivo* experiments is briefly shown in **Figure 1**. First, 3 g of PLGA (Shandong Medical Device Company, P.R. China) with an inherent viscosity of 0.6–0.8 dL/g was dissolved in 10 mL of dichloromethane (DCM). Then, 3 g of β-TCP was added to prepare PLGA/DCM solution, which was subject to a 20-min ultra-sonication. After that, 200 μg of HA15 was added to 1.5 ml of deionized water to form an aqueous solution. The HA15 aqueous solution was mixed with β-TCP/PLGA/DCM composite solution with the assistance of ultra-sonication to form uniform HA15/water/TCP/PLGA/DCM composite emulsions as printing inks. The inks were subsequently added into a 20 mL syringe connected to a V-shape nozzle (inner diameter: 0.4 mm). A pre-designed STL file shown in **Figure 2D and E** with dimensions of sample and multi-section views was imported in a cryogenic 3D printer (Shenzhen Creality 3D Technology Co., Limited, P.R. China) and cylindrical scaffolds with 3D grid patterns were printed. The printing procedure was carried out according to the pre-set parameters; the feed speed was 0.005 mL/s and the printing speed was 8 mm/s. Finally, a cylindrical scaffold with a diameter of 4 mm and a height of 15 mm were obtained (**Figure 2**). The printed scaffolds were freeze-dried for 24 h to remove all DCM.

2.2. Detection using scanning electron microscope

Scanning electron microscopy (SEM) (TESCAN-Vega 3 system) was used to observe the pore structure and micro-morphology of the prepared 3D-printed scaffold as well as the scaffold aperture size, pore connectivity, and surface morphology of pore walls. The Nano Measurer 1.2 was used to perform aperture measurement on the SEM micrograph of the bracket. In this regard, 30 measurement holes were randomly selected to calculate the mean and standard deviations (SD) to make a preliminary assessment of the aperture range.

2.3. Mechanical properties of scaffolds

An electronic universal testing machine was used to test the mechanical response of the bone tissue scaffolds with a dimension of 15 mm × 3 mm × 2 mm according to the GB/T1041-1992 Chinese standard protocol. The prepared sample was inserted in the testing area and the compression loading was conducted with a speed of 0.5 mm/min until the complete deformation, then the strength and modulus of the scaffold were measured.

2.4. *In vitro* experiments

(1) Cell culture

Murine mesenchymal stem cell line C3H10 was incubated under the standard condition in DMEM medium supplemented with 10% fetal bovine serum, 100 U/ml penicillin G, and 100 mg/ml streptomycin. To seed the C3H10 cells onto the 3D-printed scaffolds, the scaffolds were sterilized with ultraviolet light and 70% ethanol and were placed in 24-well tissue culture plates. For cell seeding, samples were pre-soaked in DMEM complete culture medium for 24 h. Subsequently, 1 mL complete culture medium (3×10^4 C3H10 cells) was poured on the top surface of the scaffolds. Then, the samples were incubated for 2 h to permit the cells to attach the scaffolds. The cells were stimulated with two concentrations of leaching solution from β-TCP/PLGA/HA15 scaffolds; the scaffold was infiltrated with 5 ml (HA15-1) or 10 ml (HA15-2) culture medium for 48 h.

(2) siRNA knockdown

We transiently transfected C3H10T1/2 cells with HSPA5 siRNA using Lipofectamine RNAiMAX (Invitrogen, Carlsbad, CA, USA) in Opti-MEM medium (Invitrogen), according to the manufacturer's instructions. The sequences of HSPA5 siRNA are as follows: Forward, 5'-AAGGUUACCCAUGCAGUUGTT-3' and reverse, 5'-AGAUUCAGCAACUGGUUAAAGTT-3'. Universal Non-targeting Control siRNA was considered and used as the control for non-sequence-specific effects. The capability of siRNA knockdown was evaluated by Western blotting. Each experiment was performed in triplicates.

(3) Western blot analysis

Cells were lysed in 2% sodium dodecyl sulfate (SDS) with 2 M urea, 10% glycerol, 10 mM Tris–

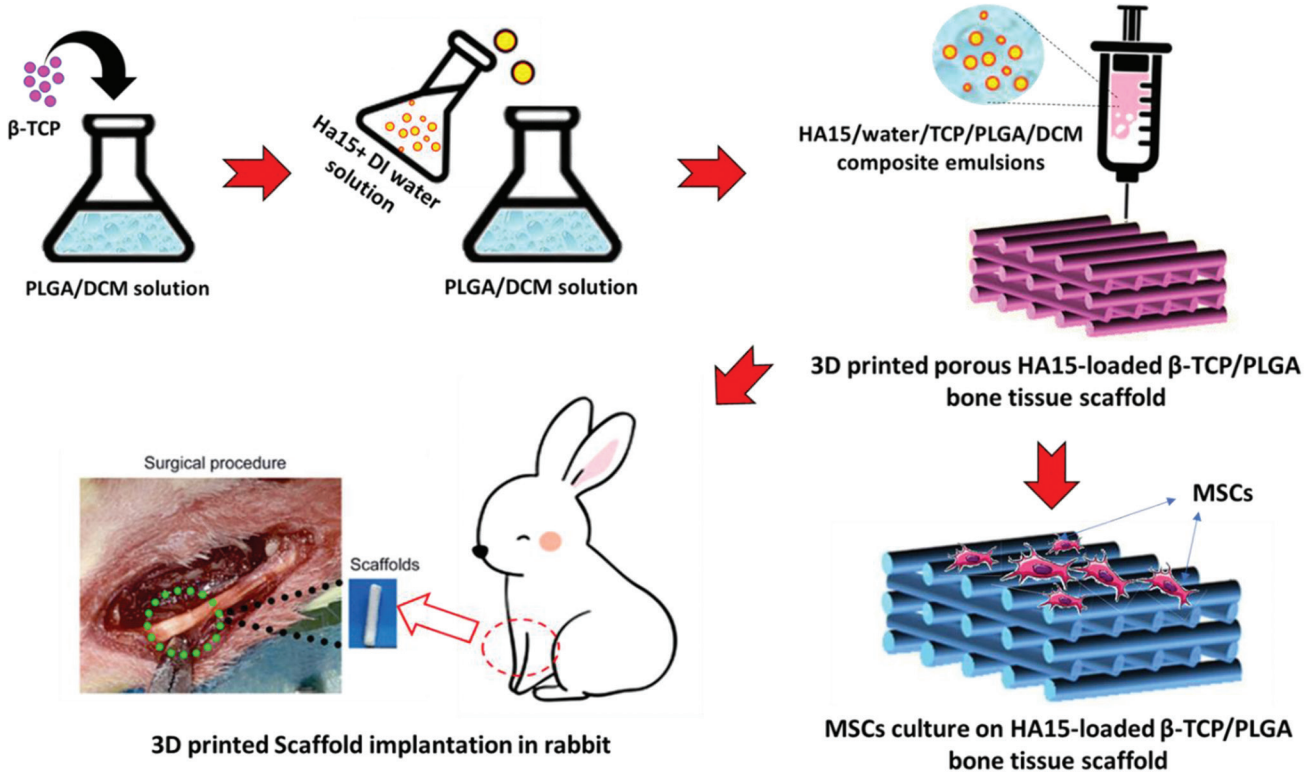

Figure 1. Production procedure of 3D-printed porous HA15-loaded β-tricalcium phosphate/poly (Lactic-co-glycolic acid) bone tissue scaffold along with *in vitro* mesenchymal stem cells (MSCs) culture and *in vivo* scaffold implantation in rabbit.

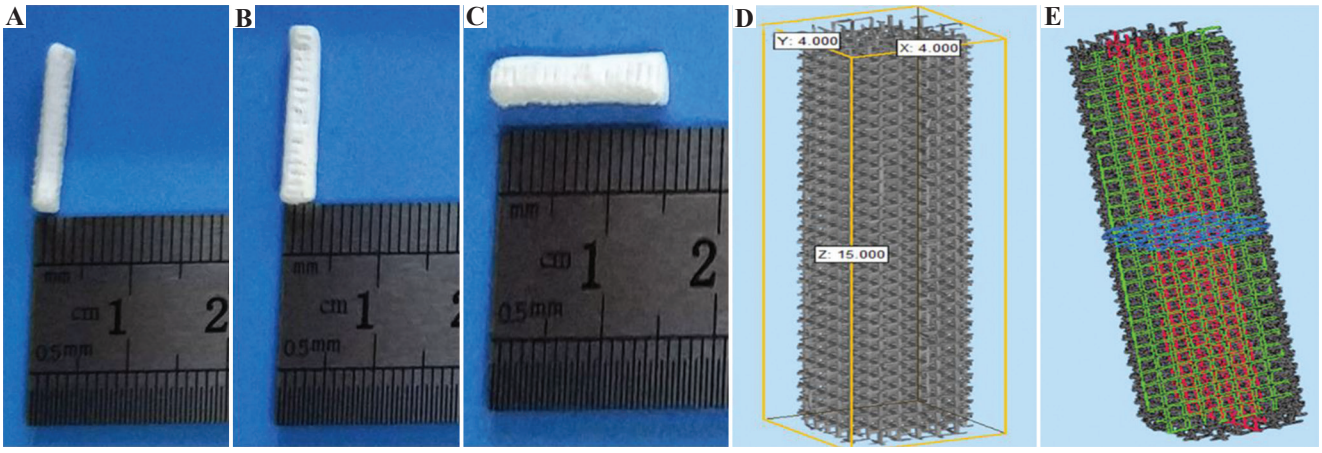

Figure 2. Prepared scaffolds. (A) β-tricalcium phosphate/poly (Lactic-co-glycolic acid)β-(TCP/PLGA) and (B) β-TCP/PLGA/HA15 samples; (C) the length of scaffolds; (D) pre-designed STL files showing the dimensions in mm; (E) STL file showing the multiple sections of sample: red for X section, green Y section, and blue for Z section.

HCl (pH 6.8), 10 mM dithiothreitol, and 1 mM phenylmethylsulfonyl fluoride. Proteins were separated by 10% SDS-polyacrylamide gel electrophoresis. After electrophoresis, proteins were transferred onto the membranes (Bio-Rad Laboratories, Hercules, CA, USA) using the wet transfer method. Each membrane was blocked using TBST (100 mM Tris–HCl pH 7.5, 150 mM NaCl, and 0.05% Tween 20) and 5% non-fat dried milk for 1 h at room temperature, and incubated with primary antibodies overnight on a shaker at 4°C. The membrane was incubated with HRP-coupled secondary antibody for 1 h at room temperature. Following this, membranes were treated with enhanced chemiluminescence reagents (ECL Kit, Amersham Biosciences, Piscataway, NJ, USA) and the proteins were detected using chemiluminescence technique.

(4) Gene expression and real-time polymerase chain reaction (PCR) analysis

The expression of osteogenic genes, including OCN, HSPA5, bone morphogenetic protein 2 (BMP2), alkaline phosphatase (ALP), collagen type I (col1a1), transcription factor Sp7 (Osterix), and Runx2, in C3H10 cells cultured on various specimens was analyzed by real-time PCR assay. After culturing for 7 days, total RNA was extracted using Trizol reagent from cells. The concentration of RNA was measured by a NanoDrop spectrophotometer (Thermo Fisher Scientific, USA). The primers used are shown in **Table 1**.

(5) Alizarin red S staining

Following osteogenic induction for 14 days, the cells were placed in 48-well plates (3-wells for each group) and fixed with 4% paraformaldehyde (PFA) for 20 min, and then rinsed twice with phosphate buffered saline (PBS). After that, the cells were stained using 40 mM alizarin red working solution for 10 min at room temperature. The cells were then rinsed twice with PBS and visualized under a light microscope. Next, 100 mmol/l cetylpyridinium chloride was poured into each well and semi-quantitative analyses were done by optical density measurement at 560 nm.

(6) Immunofluorescence analysis

For immunofluorescence analysis, after incubation with primary antibodies, followed by Alexa Fluor 594 donkey anti-mouse IgG1 (Life Technologies, Carlsbad, CA, USA) and Alexa Fluor 488 goat anti-mouse IgG2b (Life Technologies) secondary antibodies, cells were washed 3 times in PBS, after which nuclei were counterstained with 4',6-diamidino-2-phenylindole (Life Technologies). Images were obtained on a confocal laser-scanning microscope (Olympus, Tokyo, Japan).

2.5. *In vivo* experiments

(1) Radial defect treatment of rabbit

All *in vivo* animal experiments were conducted under the "Regulations on the Administration of Laboratory Animals" approved by the State Council, issued by the National Science and Technology Commission and approved by the Experimental Animal Ethics Committee of Youjiang Nationalities Medical College. Six New Zealand white rabbits, with an average weight of 2.5 ± 0.5kg, that were used in this experiment were provided by the Science Experiment Center of Youjiang Nationalities Medical College. Among them, the male rabbits and female rabbits were divided into β-TCP/groups using the random number method; these groups were PLGA/HA15 group, β-TCP/PLGA group, and bone defect group. The rabbits were assigned to either left or right radial defect model group using the random numbering method. The rabbits were anesthetized with 3% pentobarbital sodium at 20 mg/kg through ear intravenous injection (**Figure 3A**). The rabbits were fixed in the supine position and the forearm hairs were shaved to reveal the surgery site, which was disinfected with 2% iodine tincture 3 times. About 75% alcohol was used for deiodination. The corneal reflex of animals was observed to check if they were ready for surgery. The surgery began with a 2.0 cm long incision parallel to the radius of the forearm in the middle and upper segment of the forearm. Then, the subcutaneous tissue and muscle space were separated to expose the radius, after that the periosteum of the radius was cut (**Figure 3B**). An orthopedic mini-drill was used to cut a radius of about 1.5 cm in the upper-middle segment of the radius, and then the surgical site was rinsed with 0.9% sodium chloride solution. The samples were implanted at this site (indicated by a circle in **Figure 3C**). The subcutaneous tissue was sewed with 4-0 absorbable risk (**Figure 3D**). The incision was sutured with No. 0 suture and the wound was then disinfected and bandaged. The rabbits were kept in separate cages and each was administered an intramuscular penicillin injection at a dose of 1.6×10^6 units/day for 3 days post-surgery. All the animals were sacrificed 12 weeks after surgery by air embolization at the ear's marginal vein. The original surgical site was incised to observe the healing condition of the local bone defects. The surgical process is shown in **Figure 3**.

(2) Micro-computed tomography (micro-CT) scan

All experimental animals were subjected to 40-row micro-CT scanning through SIEMENS Inveon MMCT micro-CT instrument with working parameters of voltage and power of 55 kV and 80 W, respectively. Furthermore, the 3D reconstruction examination of the surgical sites was performed 12 weeks after surgery to thoroughly clarify the specific and intuitive bone callus growth and healing condition at the bone defect. Moreover, the quantitative analysis of bone volume/total volume (BV/TV), bone mineral density, trabecular thickness, and the structural model index was done according to the Hedberg's standard for evaluating the condition of new bone area.

(3) Microfil angiography and micro-CT imaging

The anesthetizing procedure was carried out according to a previously described method. The abdomen was fixed upward on the plate and the skin and muscle layer was cut along the midline of the abdomen. Then, the diaphragm was cut and the heart was exposed afterward. The heart was fixed with hemostatic forceps, and inserted with a 23G needle. The right atrial appendage in the left ventricle was cut with ophthalmic scissors. Subsequently, the infusion

Table 1. Primer sequences of osteogenic genes

Osteogenic genes	Primer sequences
HSPA5	F: 5'-CACGGTCTTTGACGCCAAG-3' R: 5'-CCAAATAAGCCTCAGCGGTTT-3'
ALP	F: 5'-CGGATCCTGACCAAAAACC-3' R: 5'-TCATGATGTCCGTGGTCAAT-3'
BMP2	F: 5'-GAATGACTGGATCGTGGCACCTC-3' R: 5'-GGCATGGTTAGTGGAGTTCAGGTG-3'
Col1α1	F: 5'-CATGTTCAGCTTTGTGGACCT-3' R: 5'-GCAGCTGACTTCAGGGATGT-3'
OCN	F: 5'-CACCATGAGGACCCTCTCTC-3' R: 5'-TGGACATGAAGGCTTTGTCA-3'
Osterix	F: 5'-TCTCCATCTGCCTGACTCCT-3' R: 5'-AGCGTATGGCTTCTTTGTGC-3'
Runx2	F: 5'-GACTGTGGTTACCGTCATGGC-3' R: 5'-ACTTGGTTTTTCATAACAGCGGA-3'
GAPDH	F: 5'-CATGTACGTTGCTATCCAGGC-3' R: 5'-CTCCTTAATGTCACGCACGAT-3'

F, forward; R, reverse; BMP2, bone morphogenetic protein 2; ALP, alkaline phosphate; col1a1, collagen type I; OCN; osteocalcin.

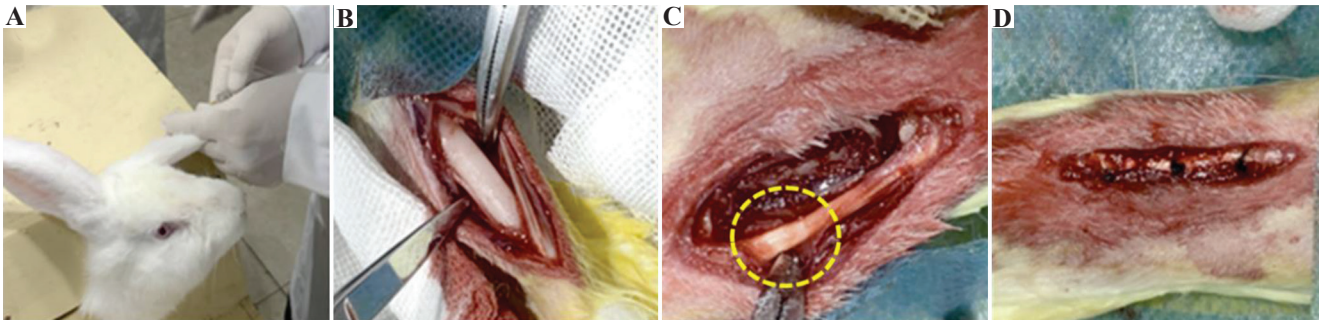

Figure 3. Surgery process on rabbit model. (A) Ear intravenous injection for anesthesia; (B) radius of the forearm in the middle and upper segment of the forearm; (C) sample implantation; (D) stitched wound.

pump was turned on and irrigated with saline until no red liquid flows out, and then it was changed to 4% PFA.

After the muscle tissue was fixed, the perfusion of 40-50 ml of mixed microfil liquid (solvent: solute=4:5, 1–2% coagulant added) was started. At the end of the perfusion process, the small blood vessels of the mesentery appeared yellow. Then, the rabbit corpse was placed in a 4°C refrigerator overnight. After the contrast agent was fixed, the rabbit upper limb was extracted to implement a micro-CT scan and observe the angiography.

2.6. Statistical analysis

The obtained results were expressed as mean ± SD. All the quantitative data were obtained from three or four independent experiments. The statistical analysis was performed using one-way analysis of variance followed by post-hoc tests. A value of $P < 0.05$ was regarded as significant.

3. Results and discussion

3.1. Characterizations of scaffolds

The pore structure of the 3D-printed scaffolds was evaluated using SEM. **Figure 4** shows the SEM micrographs of β-TCP/PLGA and β-TCP/PLGA/HA15 scaffolds. Both samples have 3D interconnected macropores with an acceptable shape tolerance and uniformity[36]. It can be observed that the number of distortions and defects is negligible and the 3D printing process has a good capability to produce this type of layer-by-layer β-TCP/PLGA scaffolds. The red dotted circles in **Figure 3** shows the near perfect pore morphologies. Also, the pores have rectangular shapes but are of varying sizes. The bigger pores have dimensions of about 200 μm ×180 μm while the smaller ones have dimensions in the range of ~100 μm × ~180 μm. This perfect pore structure maintains a large number of adhesion areas for cells.

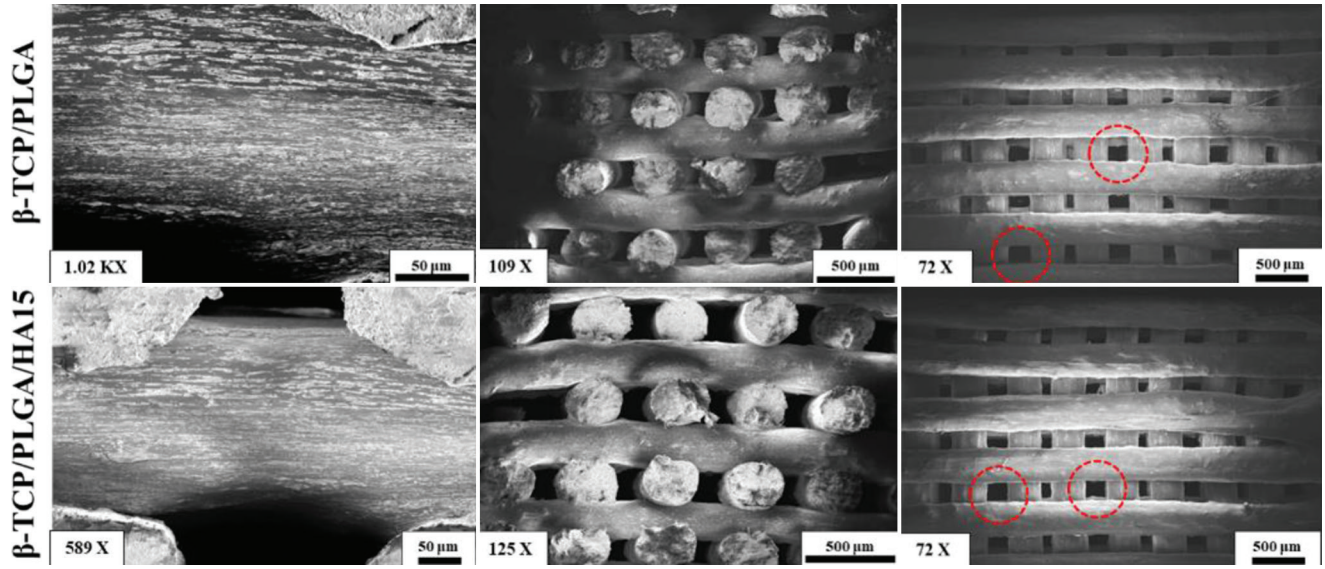

Figure 4. Scanning electron microscopy scanning results of the scaffolds with different magnifications. The upper row shows the β-tricalcium phosphate/poly (Lactic-co-glycolic acid) (β-TCP/PLGA) scaffolds and the bottom row shows the β-TCP/PLGA/HA15 scaffolds. The red dotted circles show the perfect pores.

3.2. Western blot

Figure 5A shows the qualitative western blot results of osteogenesis proteins after knockdown of HSPA5 in C3H10 cells (siRNA-transfected [Si-HSPA5]) and after being transfected with two concentrations of HA15 in stimulated osteogenic medium for 7 days. Both conditions (Si-HSPA5- and HA15-treated samples) exhibited expression for all osteogenic proteins tested, including HSPA5, OCN, Col1a1, Osterix, and β-actin. It was clearly seen that both Si-HSPA5- and HA15-treated samples did express a strong persistent signal for β-actin. Nevertheless, the Osterix has a considerable signal in both samples but it is more pronounced in Si-HSPA5. The Osterix expression is a general phenomenon in human bone tissues and Osterix as an important transcription factor is necessary for differentiation of osteoblasts[37]. Moreover, OCN as a sign of late osteoblast maturation and Col1a1 as the osteogenesis-related protein have considerably stronger signals compared to the negligible signals seen in the HA15-treated samples. It can be seen that Si-HSPA5 is more successful in silencing the HSPA5 proteins than HA15 treatment whereas HA15 can decrease the OCN and Col1a1 signals.

3.3. Gene expression

Figure 5B shows the mRNA expression of osteogenic genes in Si-HSPA5 and after 7 days treatment with two concentrations of leaching solution in C3H10 cells which is stimulated by the osteogenic medium. It was seen that all the osteogenic genes except HSPA5 were upregulated in both Si-HSPA5 and HA15 conditions compared to the control samples. The gene expression of ALP, which is an early marker of osteogenic differentiation[38], was upregulated about 3 folds in HA15-1 condition and about 0.17 fold in HA15-2 condition compared to the control sample (untreated condition and considered as natural healing). On the other hand, in the Si-HSPA condition, this increment was about 1.5 times compared to the control sample. Furthermore, the expression of OCN gene, which is a late marker of osteogenic differentiation[39], was increased for about 1.85 folds in Si-HSPA, and about 3 and 1.8 fold in HA15-2 and HA15-1 conditions, respectively. COL1A1 gene expression also showed considerable enhancement compared to control samples in all conditions. The reduction of HSPA5 in **Figure 5B** indicates a reduction of ER stress[40] and the improvement of drug performance.

3.4. Alizarin red S staining

The results of alizarin red staining showed enhanced calcium deposition in C3H10 cells that were transfected with Si-HSPA5 and two concentrations of leaching solution from β-TCP/PLGA/HA15 scaffolds on day 14, being greater in HA15-1 and Si-HSPA5 conditions (**Figure 5C**). Hence, the mineralization of extracellular matrix that usually happens during *in vitro* osteogenesis[41] can be improved by implementing HA15 and Si-HSPA5. The red spots, which serve as an indicator of calcium deposition and HA formation, considerably increased compared to control samples, indicating a better osteogenesis performance of all samples, especially the HA15-1 condition.

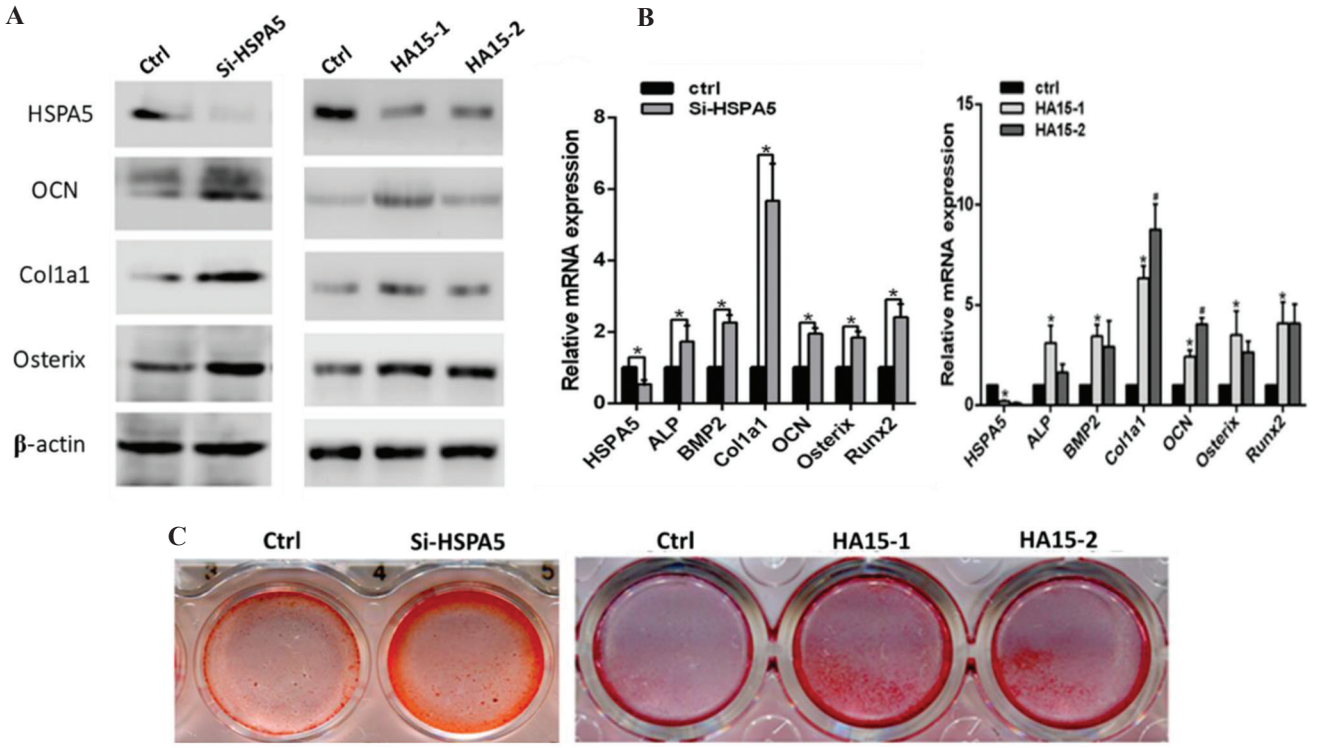

Figure 5. (A) Western blot analyses of osteogenic proteins after knockdown of HSPA5 in C3H10 cells (Si-HSPA5) and after treatment with two concentrations of leaching solution from β-tricalcium phosphate/poly (Lactic-co-glycolic acid)/HA15 scaffolds (HA15-1, HA15-2) in stimulated osteogenic medium for 7 days. (B) mRNA expression of osteogenic genes after knockdown of HSPA5, treatment with HA15-1 or HA15-2 in C3H10 cells and being stimulated by osteogenic medium for 7 days. (C) Alizarin red S staining of C3H10 cells with HSPA5 knockdown and treatment with HA15-1 or HA15-2 in osteogenic medium for 14 days.

3.5. Immunofluorescence staining

The OCN protein, DAPI, and HSPA5 were stained using immunofluorescence method and the co-localization of them was observed using confocal laser scanning microscope. The OCN proteins were marked by green fluorescence, HSPA5 by red color, and the nucleus labeled by DAPI as blue color. After merging all the immunofluorescence figures, it can be seen that OCN and HSPA5 were co-localized in cytoplasm and nucleus (**Figure 6**). Significantly stronger OCN staining was observed in the HA15 sample in comparison to the control, indicating a better osteogenic effect. Contrarily, the amount of HSPA5 was considerably decreased in the HA15 sample compared to the control. Thus, HA15 has the potential to improve osteogenesis and reduce HSAP5.

3.6. Mechanical properties

The mechanical compression performance of β-TCP/PLGA and β-TCP/PLGA/HA15 samples is listed in **Table 2** and their respective stress-strain curves are illustrated in **Figure 7**. The compression strengths of

Table 2. Compression mechanical results of β-TCP/PLGA and β-TCP/PLGA/HA15 scaffolds

Scaffold	Young modulus (E)	Ultimate tensile strength (UTS)	Strain
β-TCP/PLGA	27.86	0.366 MPa	1.28%
β-TCP/PLGA/HA15	31.36	0.443 MPa	8.6%

β-TCP/PLGA and β-TCP/PLGA/HA15 samples were about 0.366 MPa and 0.443 MPa, respectively. It can be seen that the compression strength of the β-TCP/PLGA/HA15 scaffold is 19% higher than that of the β-TCP/PLGA and is considered more suitable for load-bearing applications, especially bone defects. Although β-TCP/PLGA has less Young's modulus and can inhibit stress shielding effect, this amount in β-TCP/PLGA/HA15 is not considerably high and it can still maintain good biomechanical properties. The compression strength and Young's modulus of these samples are comparable with those of cancellous bone tissue[42,43]; hence, they seem to be suitable for bone defect applications. Nonetheless, the performance of

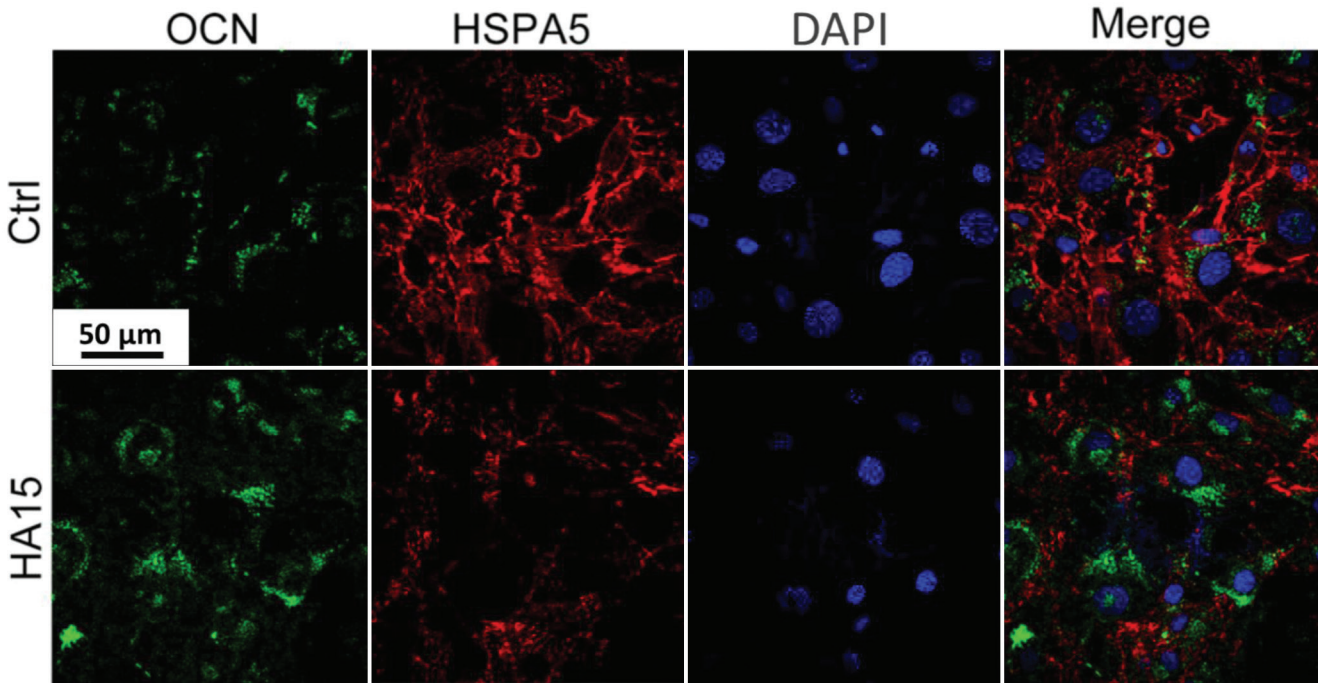

Figure 6. Immunofluorescence staining of OCN, HSPA5, and DAPI in C3H10 cells treated with leaching solution from β-tricalcium phosphate/poly (Lactic-co-glycolic acid)/HA15 scaffolds and osteogenic medium for 7 days.

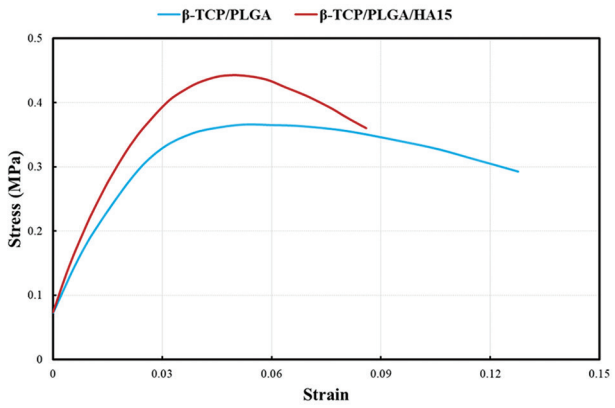

Figure 7. Mechanical compression stress-strain curve of β-tricalcium phosphate/poly (Lactic-co-glycolic acid) (β-TCP/PLGA) and β-TCP/PLGA/HA15 scaffolds.

β-TCP/PLGA/HA15 scaffold is better and should be the potential choice.

3.7. Micro-CT scan and microfil angiography of bone formation

After implantation of scaffolds and surgery procedure (**Figure 8A**), the BV fraction (%) of scaffolds was analyzed by micro-CT scan as shown in **Figure 8B**. Micro-CT scan experiment can accurately quantify the bone and its spatial growth and 3D distribution[44]. It can be seen that the samples have very different mineralization behavior. The extent of bone formation of the β-TCP/PLGA/HA15 sample was considerably higher than that of the β-TCP/PLGA and control sample 12 weeks after the surgery. The addition of HA15 considerably improved bone mineralization but the effect of β-TCP/PLGA seemed to be not significant. It should be considered that the scaffold material was mostly degraded after 12 weeks so it cannot be shown by micro-CT scans.

The 3D images of neovascularization (newly formed vessel-like structure) in the scaffold region are demonstrated in **Figure 8C**. There were considerably more newly formed vessels in the β-TCP/PLGA/HA15 and β-TCP/PLGA scaffolds compared to the control sample. The best performance was seen in the β-TCP/PLGA/HA15 sample. For more effective bone repair and regeneration, angiogenesis is essential. Moreover, vascularization leads to osteogenesis during tissue maturity and regeneration[45]. Reportedly, the neovascularization improvement could accelerate osteogenesis even before the establishment of local blood flow[46]. Hence, the formation of β-TCP/PLGA and β-TCP/PLGA/HA15 scaffolds could significantly enhanced bone regeneration. **Figure 9** shows the accumulative HA15 release profile of β-TCP/PLGA/HA15 scaffold in which it can be seen that about 73% of HA15 was released in 25 days. The rate of HA15 release was very fast in the 1st week, especially after 5 days, then it started to decrease. If the release rate of the substance was assumed to be constant after 7 days, 100% of the HA15 would be released after about 59 days.

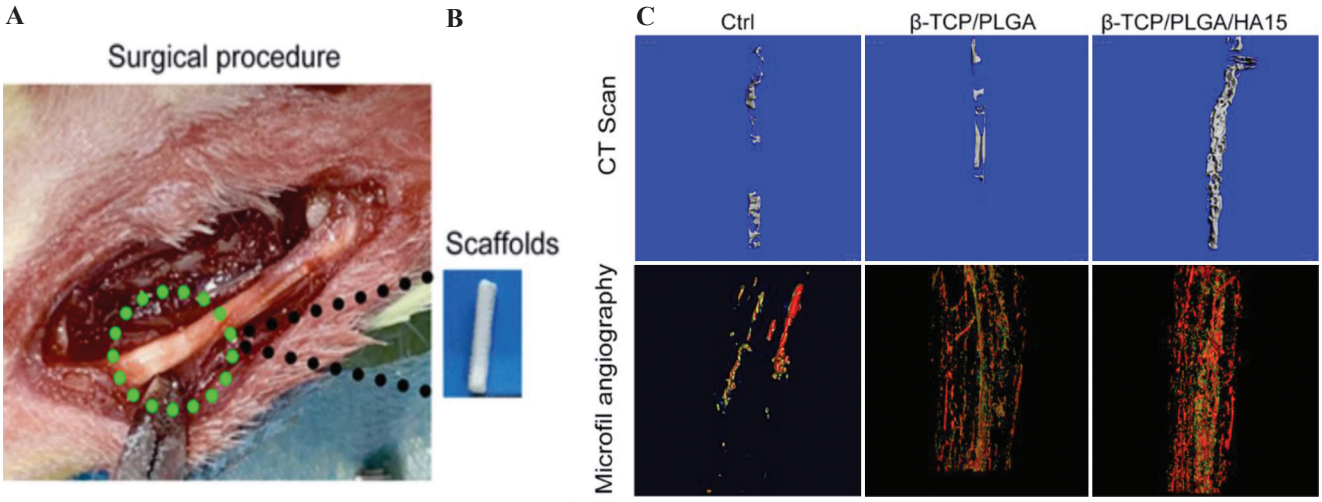

Figure 8. (A) Scaffold implantation surgical procedure in rabbits. (B) Micro-computed tomography (Micro-CT) scan images and quantification results of the defect area 12 weeks after the surgery; newly formed bone appeared as white dots on the CT images. (C) Microfil angiography and micro-CT imaging results of the rabbits.

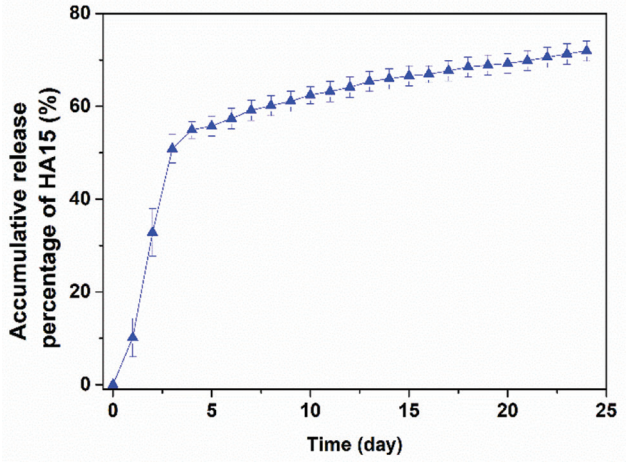

Figure 9. Accumulative HA15 release profile of β-tricalcium phosphate/poly (Lactic-co-glycolic acid)/HA15 scaffold.

4. Conclusion

In this study, a β-TCP/PLGA bone tissue scaffold loaded with osteogenesis-promoting drug HA15 was constructed by 3D printing technology. The scaffold loaded with the HA15 delivery system has favorable biomechanical properties comparable to those of the cancellous bone tissue and can promote cell differentiation into osteoblasts *in vitro* targeting HSPA5 and promote bone regeneration in a rabbit bone defect model. Moreover, this scaffold can enhance angiogenesis that has a significant role in more effective bone repair and regeneration. It was seen that HA15 can target HSPA5 to inhibit ER stress and promote osteogenesis, along with the inhibition of ER stress, reduced apoptosis, and induced autophagy *in vivo*. Overall, this study might provide a theoretical approach for the treatment of bone defects with HA15-loaded biomaterials.

Conflicts of interest

The authors declare no conflicts of interest.

References

1. Trejo-Iriarte CG, Serrano-Bello J, Gutiérrez-Escalona R, *et al*., 2019, Evaluation of Bone Regeneration in a Critical Size Cortical Bone Defect in Rat Mandible Using MicroCT and Histological Analysis. *Arch Oral Biol*, 101:165–71. https://doi.org/10.1016/j.archoralbio.2019.01.010
2. Tarafder S, Davies NM, Bandyopadhyay A, *et al*., 2013, 3D Printed Tricalcium Phosphate Bone Tissue Engineering Scaffolds: Effect of SrO and MgO Doping on *In Vivo* Osteogenesis in a Rat Distal Femoral Defect Model. *Biomater Sci*, 1:1250. https://doi.org/10.1039/c3bm60132c
3. Giannoudis PV, Dinopoulos H, Tsiridis E, 2005, Bone Substitutes: An Update. *Injury*, 36:S20–7. https://doi.org/10.1016/j.injury.2005.07.029
4. Pape HC, Evans A, Kobbe P, 2010, Autologous Bone Graft: Properties and Techniques. *J Orthop Trauma*, 24:S36–40. https://doi.org/10.1097/BOT.0b013e3181cec4a1
5. Ebraheim NA, Elgafy H, Xu R, 2001, Bone-Graft Harvesting From Iliac and Fibular Donor Sites: Techniques and Complications. *J Am Acad Orthop Surg*, 9:210–8. https://doi.org/10.5435/00124635-200105000-00007
6. Arrington ED, Smith WJ, Chambers HG, *et al*., 1996, Complications of Iliac Crest Bone Graft Harvesting. *Clin Orthop Relat Res*, 329:300–9. https://doi.org/10.1097/00003086-199608000-00037

7. Burg KJ, Porter S, Kellam JF, 2000, Biomaterial Developments for Bone Tissue Engineering. *Biomaterials*, 21:2347–59. https://doi.org/10.1016/S0142-9612(00)00102-2
8. Khojasteh A, Fahimipour F, Eslaminejad MB, *et al*., 2016, Development of PLGA-coated β-TCP Scaffolds Containing VEGF for Bone Tissue Engineering. *Mater Sci Eng C*, 69:780–8. https://doi.org/10.1016/j.msec.2016.07.011
9. Yang S, Leong KF, Du Z, *et al*., 2001, The Design of Scaffolds for Use in Tissue Engineering. Part I. Traditional Factors. *Tissue Eng*, 7:679–89. https://doi.org/10.1089/107632701753337645
10. Ng WL, Chua CK, Shen YF, 2019, Print me an Organ! Why we are not there YET. *Prog Polym Sci*, 97:101145. https://doi.org/10.1016/j.progpolymsci.2019.101145
11. Zhou H, Lawrence JG, Bhaduri SB, 2012, Fabrication Aspects of PLA-CaP/PLGA-CaP Composites for Orthopedic Applications: A Review. *Acta Biomater*, 8:1999–2016. https://doi.org/10.1016/j.actbio.2012.01.031
12. Hollister SJ, 2009, Scaffold Design and Manufacturing: From Concept to Clinic. *Adv Mater*, 21:3330–42. https://doi.org/10.1002/adma.200802977
13. Badekila AK, Kini S, Jaiswal AK, 2020, Fabrication Techniques of Biomimetic Scaffolds in Three-dimensional Cell Culture: A Review. *J Cell Physiol*, 2020:29935. https://doi.org/10.1002/jcp.29935
14. Logeart-Avramoglou D, Anagnostou F, Bizios R, *et al*., 2005, Engineering Bone: Challenges and for Bone Tissue Engineering and Regenerative Medicine: A Review. *J Cell Mol Med*, 9:72–84. https://doi.org/10.1111/j.1582-4934.2005.tb00338.x
15. Pina S, Oliveira JM, Reis RL, 2015, Natural-Based Nanocomposites. *Adv Mater*, 27:1143–69. https://doi.org/10.1002/adma.201403354
16. Asti A, Gioglio L, 2014, Natural and Synthetic Biodegradable Polymers: Different Scaffolds for Cell Expansion and Tissue Formation. *Int J Artif Organs*, 37:187–205. https://doi.org/10.5301/ijao.5000307
17. Shrivats AR, McDermott MC, Hollinger JO, 2014, Bone Tissue Engineering: State of the Union. *Drug Discov Today*, 19:781–86. https://doi.org/10.1016/j.drudis.2014.04.010
18. Winkler T, Sass FA, Duda GN, *et al*., 2018, A Review of Biomaterials in Bone Defect Healing, Remaining Shortcomings and Future Opportunities for Bone Tissue Engineering. *Bone Joint Res*, 7:232–43. https://doi.org/10.1302/2046-3758.73.BJR-2017-0270.R1
19. Nandi SK, Fielding G, Banerjee D, *et al*., 2018, 3D-Printed β-TCP Bone Tissue Engineering Scaffolds: Effects of Chemistry on *In Vivo* Biological Properties in a Rabbit Tibia Model. *J Mater Res*, 33:1939–47. https://doi.org/10.1557/jmr.2018.233
20. Liu Q, Cen L, Yin S, *et al*., 2008, A Comparative Study of Proliferation and Osteogenic Differentiation of Adipose-derived Stem Cells on Akermanite and β-TCP Ceramics. *Biomaterials*, 29:4792–99. https://doi.org/10.1016/j.biomaterials.2008.08.039
21. Gentile P, Chiono V, Carmagnola I, *et al*., 2014, An Overview of Poly(lactic-co-glycolic) Acid (PLGA)-Based Biomaterials for Bone Tissue Engineering. *Int J Mol Sci*, 15:3640–59. https://doi.org/10.3390/ijms15033640
22. Yadav RK, Chae SW, Kim HR, *et al*., 2014, Endoplasmic Reticulum Stress and Cancer. *J Cancer Prev*, 19 (2014) 75–88. https://doi.org/10.15430/JCP.2014.19.2.75.
23. Urra H, Dufey E, Avril T, *et al*., 2016, Endoplasmic Reticulum Stress and the Hallmarks of Cancer. *Trends Cancer*, 2:252–62. https://doi.org/10.1016/j.trecan.2016.03.007
24. Díaz-Villanueva J, Díaz-Molina R, García-González V, 2015, Protein Folding and Mechanisms of Proteostasis. *Int J Mol Sci*, 16:17193–230. https://doi.org/10.3390/ijms160817193
25. Sano R, Reed JC, 2013, ER Stress-induced Cell Death Mechanisms. *Biochim Biophys Acta Mol Cell Res*, 1833:3460–70. https://doi.org/10.1016/j.bbamcr.2013.06.028
26. Attarilar S, Yang J, Ebrahimi M, *et al*., 2020, The Toxicity Phenomenon and the Related Occurrence in Metal and Metal Oxide Nanoparticles: A Brief Review From the Biomedical Perspective. *Front Bioeng Biotechnol*, 8:822. https://doi.org/10.3389/fbioe.2020.00822
27. Cerezo M, Lehraiki A, Millet A, *et al*., 2016, Compounds Triggering ER Stress Exert Anti-Melanoma Effects and Overcome BRAF Inhibitor Resistance. *Cancer Cell*, 29:805–19. https://doi.org/10.1016/j.ccell.2016.04.013
28. Xiao G, Jiang D, Ge C, *et al*., 2005, Cooperative Interactions between Activating Transcription Factor 4 and Runx2/Cbfa1 Stimulate Osteoblast-specific Osteocalcin Gene Expression. *J Biol Chem*, 280:30689–96. https://doi.org/10.1074/jbc.M500750200
29. Wang W, Chen J, Hui Y, *et al*., 2018, Down-Regulation of miR-193a-3p Promotes Osteoblast Differentiation through up-regulation of LGR4/ATF4 Signaling. *Biochem Biophys Res Commun*, 503:2186–93. https://doi.org/10.1016/j.bbrc.2018.08.011

30. Zhang K, Kaufman RJ, 2004, Signaling the Unfolded Protein Response from the Endoplasmic Reticulum. *J Biol Chem*, 279:25935–8. https://doi.org/10.1074/jbc.R400008200
31. Ni M, Lee AS, 2007, ER Chaperones in Mammalian Development and Human Diseases. *FEBS Lett*, 581:3641–51. https://doi.org/10.1016/j.febslet.2007.04.045
32. Macario L, Alberto J, 2007, Molecular Chaperones: Multiple Functions, Pathologies, and Potential Applications. *Front Biosci*, 12:2588. https://doi.org/10.2741/2257
33. Hasnain SZ, Lourie R, Das I, *et al*., 2012, The Interplay between Endoplasmic Reticulum Stress and Inflammation. *Immunol Cell Biol*, 90:260–70. https://doi.org/10.1038/icb.2011.112
34. Chen Y, Mi Y, Zhang X, *et al*., 2019, Dihydroartemisinin-Induced Unfolded Protein Response Feedback Attenuates Ferroptosis via PERK/ATF4/HSPA5 Pathway in Glioma Cells. *J Exp Clin Cancer Res*, 38:402. https://doi.org/10.1186/s13046-019-1413-7
35. Uckun FM, Qazi S, Ozer Z, *et al*., 2011, Inducing Apoptosis in Chemotherapy-Resistant B-Lineage Acute Lymphoblastic Leukaemia Cells by Targeting HSPA5, a Master Regulator of the Anti-apoptotic Unfolded Protein Response Signalling Network. *Br J Haematol*, 153:741–52. https://doi.org/10.1111/j.1365-2141.2011.08671.x
36. Touri M, Kabirian F, Saadati M, *et al*., 2019, Additive Manufacturing of Biomaterials the Evolution of Rapid Prototyping. *Adv Eng Mater*, 21:1800511. https://doi.org/10.1002/adem.201800511
37. Nakashima K, Zhou X, Kunkel G, *et al*., 2002, The Novel Zinc Finger-Containing Transcription Factor Osterix is Required for Osteoblast Differentiation and Bone Formation. *Cell*, 108:17–29. https://doi.org/10.1016/S0092-8674(01)00622-5
38. Pirraco RP, Reis RL, Marques AP, 2013, Effect of Monocytes/Macrophages on the Early Osteogenic Differentiation of hBMSCs. *J Tissue Eng Regen Med*, 7:392–400. https://doi.org/10.1002/term.535
39. Catelas I, Sese N, Wu BM, *et al*., 2006, Human Mesenchymal Stem Cell Proliferation and Osteogenic Differentiation in Fibrin Gels *In Vitro*. *Tissue Eng*, 12:2385–96. https://doi.org/10.1089/ten.2006.12.2385
40. Scheiber AL, Guess AJ, Kaito T, *et al*., 2019, Endoplasmic Reticulum Stress is Induced in Growth Plate Hypertrophic Chondrocytes in G610C Mouse Model of Osteogenesis Imperfecta. *Biochem Biophys Res Commun*, 509:235–40. https://doi.org/10.1016/j.bbrc.2018.12.111
41. Tataria M, Quarto N, Longaker MT, *et al*., 2006, Absence of the p53 Tumor Suppressor Gene Promotes Osteogenesis in Mesenchymal Stem Cells. *J Pediatr Surg*, 41:624–632. https://doi.org/10.1016/j.jpedsurg.2005.12.001
42. Gerhardt LC, Boccaccini AR, 2010, Bioactive Glass and Glass-Ceramic Scaffolds for Bone Tissue Engineering. *Materials* (*Basel*), 3:3867–910. https://doi.org/10.3390/ma3073867
43. Nazarian A, von Stechow D, Zurakowski D, *et al*., 2008, Bone Volume Fraction Explains the Variation in Strength and Stiffness of Cancellous Bone Affected by Metastatic Cancer and Osteoporosis. *Calcif Tissue Int*, 83:368–79. https://doi.org/10.1007/s00223-008-9174-x
44. Lee JY, Son SJ, Son JS, *et al*., 2016, Bone-Healing Capacity of PCL/PLGA/Duck Beak Scaffold in Critical Bone Defects in a Rabbit Model. *Biomed Res Int*, 2016:1–10. https://doi.org/10.1155/2016/2136215
45. Collin-Osdoby P, 1994, Role of Vascular Endothelial Cells in Bone Biology. *J Cell Biochem*, 55:304–9. https://doi.org/10.1002/jcb.240550306
46. Chen SH, Lei M, Xie XH, *et al*., 2013, PLGA/TCP Composite Scaffold Incorporating Bioactive Phytomolecule Icaritin for Enhancement of Bone Defect Repair in Rabbits. *Acta Biomater*, 9:6711–22. https://doi.org/10.1016/j.actbio.2013.01.024